Landslides (2021) 18:79–88
DOI 10.1007/s10346-020-01471-x
Received: 14 November 2019
Accepted: 22 June 2020
Published online: 18July 2020

Guoqing Chen · Peng Tang · Runqiu Huang · Dong Wang · Zhiheng Lin · Da Huang

Critical tension crack depth in rockslides that conform to the three-section mechanism

Abstract The three-section mechanism is a typical mechanism of large-scale rockslides. Such rockslides are typically characterized by sudden instability and can cause many casualties and considerable economic losses due to their high-speed and long-distance runout. Their evolutionary process is closely related to the development of the tension crack at the trailing edge and the sudden brittle failure of the locked section. In this study, the curved failure path of the locked section was verified by means of the numerical simulation conducted using PFC^{2D}. On the basis of that, the critical threshold of the tension crack depth for slope instability was derived based on the limit equilibrium state determined using the vector sum method, and this threshold was then verified through application in a case study. The results show that the critical tension crack depth threshold is not only related to the slope height but also closely related to other geometric and mechanical parameters of the slope. In addition, the case study shows that the result calculated using the methodology proposed in this paper is more accurate than that obtained from the previous empirical equation. Hence, the outcomes of this study are significant for improving stability analyses, instability prediction, and the early warning of instability for such rockslides.

Keywords Rockslides · Three-section mechanism · Tension crack · Critical depth · Instability prediction and early warning

Introduction

The three-section mechanism is the underlying mechanism of a typical geomechanical model for large-scale rockslides. In this model, the sliding surface is directly determined by three sections (Fig. 1): (a) the creep section along the weaker strata, (b) the steep tension section along the tension crack at the rear, and (c) the curved locked section in between (Huang 2009; Huang 2012). During the evolution of such a rockslide, the sliding at the slope toe driven by continuous creep deformation causes the initiation of a tension crack from the head of the slope that then propagates farther into the body of the slope until shear failure of the locked section occurs.

Evidently, the evolutionary process of this type of rockslide is closely related to the development of the tension crack at the trailing edge; hence, this crack development is a vital concern for real-time monitoring and early warning. Since these rockslides typically occur suddenly, as determined by the brittle shear failure of the locked section when the tension crack reaches a certain depth, the high-speed and long-distance runout of such a rockslide usually results in many casualties and considerable economic losses (Zhang and Liu 1990; Huang et al. 1991; Huang and Deng 1993; Sartori et al. 2003; Eberhardta et al. 2004).

For a rockslide that conforms to the three-section mechanism, the instability of the slope is almost impossible to predict on the basis of displacement monitoring at the surface and in the interior of the slope due to the lack of a regular progressive deformation pattern (i.e., initial, stable, and accelerating deformation) in the slope displacement curve. Therefore, due to the suddenness of these rockslides, it is difficult to provide early warning of their instability. To solve this difficulty, the critical tension crack depth was summarized according to the following empirical equation shown in Eq. (1) based on rockslides conforming to the three-section mechanism (Zhang and Liu 1990) and was recommended for predicting the instability of such rockslides (Huang and Deng 1993; Huang 2012).

$$H_{cr} = 0.5763H - 27.0992 \tag{1}$$

Although Eq. (1) correctly reflects the actual observation that the critical depth of the tension crack for slope instability is approximately half of the slope height, this equation was derived from an empirical summary of rockslides and lacks a theoretical basis. Therefore, it cannot yield highly accurate calculation results for all rockslides that conform to the three-section mechanism.

To improve the calculation accuracy of the critical tension crack depth, it is critical to explore the failure path of the locked section. The 2D Particle Flow Code (PFC^{2D}), as one of discrete element methods, represents the rock mass as an assembly of bonded particles, and it directly allows crack initiation and propagation by bond breakage between the particles of the locked section (Huang et al. 2015). Therefore, PFC^{2D} has natural advantages to investigate the potential failure path of the locked section. In this paper, the failure path of the locked section is verified by the numerical simulation using PFC^{2D}, the results of which indicate that this failure path can be assumed to follow an arc that is tangent to both the tension crack and the creep section. On this basis, a critical tension crack depth threshold is derived based on the limit equilibrium state determined via the vector sum method (VSM) proposed by Ge (2008), and this threshold is then verified through application in a case study. The results show that the critical tension crack depth in a rockslide that conforms to the three-section mechanism is a function of the geometric and mechanical parameters of the slope. The outcomes of this study are significant for improving stability analyses, instability prediction, and early warning for such rockslides.

Verification of the failure path of the locked section

For a rockslide that conforms to the three-section mechanism, the failure path of the locked section serves as a vital foundation for analyzing the slope stability and estimating the critical depth of the rear tension crack for instability. Field investigation results show that the sliding surface morphology of the locked section in the middle is approximately circular instead of a straight-line path (Huang et al. 1991). To verify this finding, a numerical simulation was performed to investigate the failure path of the locked section as determined by the self-weight of the slope by employing the Particle Flow Code (PFC), in which the rock mass was represented as an assemblage of bonded rigid disk-shaped particles based on the principles of the discrete element method (DEM) (Huang et al.

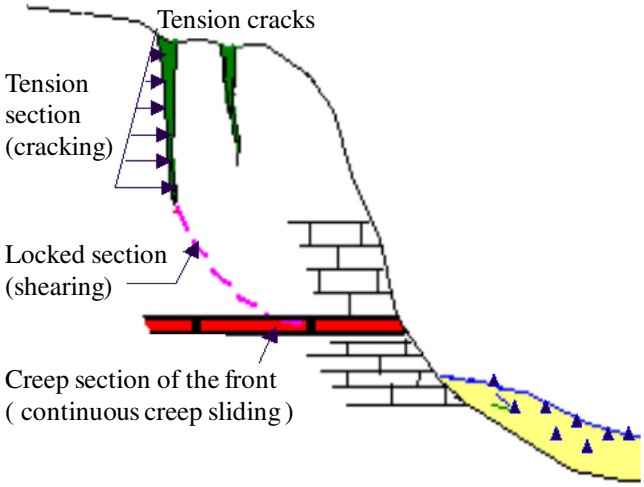

Fig. 1 The three-section model and its features (Huang 2012): (a) brittle rock, or rock and soil, with nearly horizontal or gently inclined structural planes at the toe of the slope and (b) hard rock with thin interlayers of weaker material

2015). The mechanical behavior of the particles in such an assemblage obeys Newton's second law. The force and moment acting at each contact bond between particles are described by the force-displacement law (Itasca Consulting Group Inc. 2016).

In this study, the slope materials were assumed to be homogeneous and were simulated using the parallel bond model shown in Fig. 2, which is subject to a normal force, shear forces, and a rotation moment. Thus, the concentration of the internal forces may cause the bond in this model to break in either a tension mode or a shear mode, simulating the rupture of real geotechnical materials (Cho et al. 2007). The microparameters shown in Table 1 were obtained based on the calibration for the target macroscopic parameters shown in Table 2, which came from a real rockslide that conforms to the three-section mechanism (Huang et al. 1991). The abovementioned calibration of the microparameters was completed by the corresponding numerical tests: the standard uniaxial compressive test for the uniaxial compressive strength, Poisson's ratio, and Young's modulus of the locked section; the direct shear tests with the normal stresses of 4, 5, 6, 7, and 8 MPa for the internal friction angle and cohesion of the locked section; and the direct shear tests with normal stresses of 0.22, 0.23, 0.24, 0.25, and 0.26 MPa for the internal friction angle and cohesion of the creep section. The radius of the particles for all of the numerical tests was set as 0.5~0.75 mm, and the numerical models for the direct shear tests were a 100 mm height and a 100 mm width.

The PFC^{2D} slope model contains 45,121 particles with a radius of 0.1~0.15 m, and its geometric dimensions can be found in Fig. 2. The origin of the coordinate system is located at the lower left corner point of the model. The positive directions of the x-axis and y-axis point to the right and in the upward direction, respectively. A prefabricated crack with a length of 20 m, as shown in Fig. 2, was created by deleting the corresponding disk particles (Yang et al. 2014). The creep section at the slope toe with the width of 0.2 m, as shown in green in Fig. 2, was created employing the smooth joint model, in which the behavior of a structural plane with dilation, regardless of the local particle contact orientations, is simulated by assigning smooth joint models to all contacts between particles that lie on opposite sides of the joint (Itasca Consulting Group Inc 2016). Considering the great difference in the peak and residual strengths in the locked section (Tang et al. 2020), the limit state corresponding to the failure of the locked section was simulated by enhancing the acceleration of gravity by a factor of 10, which is similar to the slope safety factor by the method of gravity increase.

The evolutionary process of the rupture of the locked section is shown in Fig. 3. The corresponding force chains are represented by two colors: red reflects compression and blue reflects tension. The duration of the entire process, from crack initiation to ultimate failure, was 30,000 time steps. In the initial stage, compressive forces were concentrated at the tip of the prefabricated crack (Fig. 3a). Subsequent internal force redistribution caused the force state to transition from compression to tension (Fig. 3b), and the area of tension force concentration at the tip of the prefabricated crack gradually expanded (Fig. 3c). Crack initiation occurred at the prefabricated crack tip once the tension force concentration reached a certain level (Fig. 3d), and the crack then propagated with the migration of the area of tension force concentration (Fig. 3e–g). Ultimately, the crack coalesced with the creep section (Fig. 3h), causing the locked section to fail completely (Fig. 3i). The

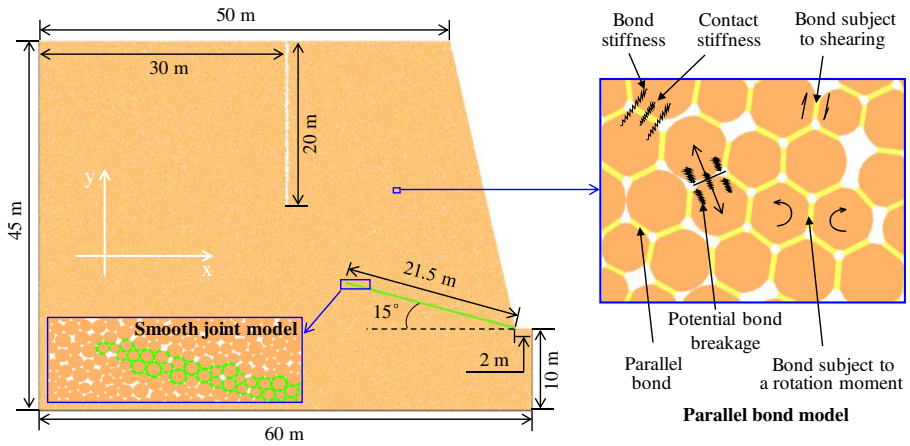

Fig. 2 Numerical simulation model in PFC^{2D}

Table 1 Microparameters used to simulate the rupture path of the locked section in this study

Parameter	Value	Parameter	Value
Density (kg/m^3)	2650	Parallel bond Young's modulus (GPa)	19.6
Porosity ratio	0.1	Parallel bond tensile strength (MPa)	32
Damping coefficient	0.7	Parallel bond cohesion (MPa)	212
Particle friction coefficient	0.577	Smooth joint normal stiffness (Pa/m)	30e6
Contact Young's modulus (GPa)	19.6	Smooth joint tangential stiffness (Pa/m)	5e6
Stiffness ratio	1.96	Smooth joint friction coefficient	0.5
Parallel bond stiffness ratio	1.96	Smooth joint tensile strength (MPa)	5

failure path of the locked section in the PFC^{2D} model was not a straight-line segment but rather a circular arc between points A and B (Fig. 4), which is consistent with the field investigation results.

Methodology for calculating the critical tension crack depth

The critical tension crack depth at the trailing edge corresponds to the limit equilibrium state of the slope. To date, two main methods have been developed for calculating slope stability based on the limit equilibrium or failure state: the limit equilibrium method (LEM) (Bishop 1955; Fredlund and Krahn 1977; Duncan 1996) and the strength reduction method (SRM) (Zienkiewicz et al. 1975; Griffiths and Lane 1999). These methods are built on many assumptions, without consideration of the actual stress state. Ge (2008) therefore proposed a method of slope stability analysis called the VSM that considers both the magnitudes and directions of the forces. The safety factor in the VSM has a clear physical meaning, i.e., the ratio of the total resisting force to the total driving force in the global sliding direction. Recently, the VSM has undergone further development and has been successfully applied for the stability analysis of slopes (Fu et al. 2017; Liu et al. 2017; Guo et al. 2018; Guo et al. 2019).

Before the VSM can be used, it is vital to identify the potential slip surface. To quantitatively analyze the failure path of the locked section, we extracted all positional coordinate points of the break bonds in the failure path of the locked section and found that they can be fitted as the equation of a circle as shown in Fig. 5, the coefficient of determination R^2 of which almost equal to 1, indicating that the failure path of the locked section can be regarded as a circular arc. The fitted coordinate of the center point O of the circle is nearly (44.6, 27.7), and the fitted radius is approximately 14.9. The angles ∠OBA and ∠OCD in Fig. 4 calculated by the fitted results are 80° and 74°, respectively (both nearly 90°), indicating that the failure path of the locked section is approximately tangent to both the creep section and the tension section. Therefore, in the landslides that conform to the three-section mechanism, the potential slip surface in the locked section can be assumed to be a circular arc that is tangent to both the creep section and the tension section. The potential slip surface composed of the creep section, the locked section, and the tension section can be clearly identified to support the analyses below.

Theoretical model

The generalized model of a rockslide that conforms to the three-section mechanism and its corresponding Cartesian coordinate system are depicted in Fig. 6a, where point O is the origin of the coordinates. The tension crack and the creep section are represented by the yellow line and the gray line, respectively. H represents the slope height shown in Fig. 6, x_d represents the distance between the tension crack and the edge of the slope face, and the dip angle of the creep section and the slope angle are represented by α and β, respectively. The coordinates of the lowest point of the tension crack are (0, y_t). The transverse coordinate x_c of the slope toe can be expressed as:

$$x_c = x_d + H\cot\beta \tag{2}$$

Table 2 Macroproperties in the PFC^{2D} models and an actual slope

	Items	Values of the PFC^{2D} models	Values in a real slope (Huang et al. 1991)
The locked section	Uniaxial compressive strength (MPa)	116.78	103.02~256.74
	Poisson's ratio	0.22	0.19~0.25
	Young's modulus (GPa)	35	32~43
	Internal friction angle (°)	48.94	47~55
	Cohesion (MPa)	20.31	15~25
The creep section	Internal friction angle (°)	29.7	26.5~30.5
	Cohesion (MPa)	0.49	0.21~0.49

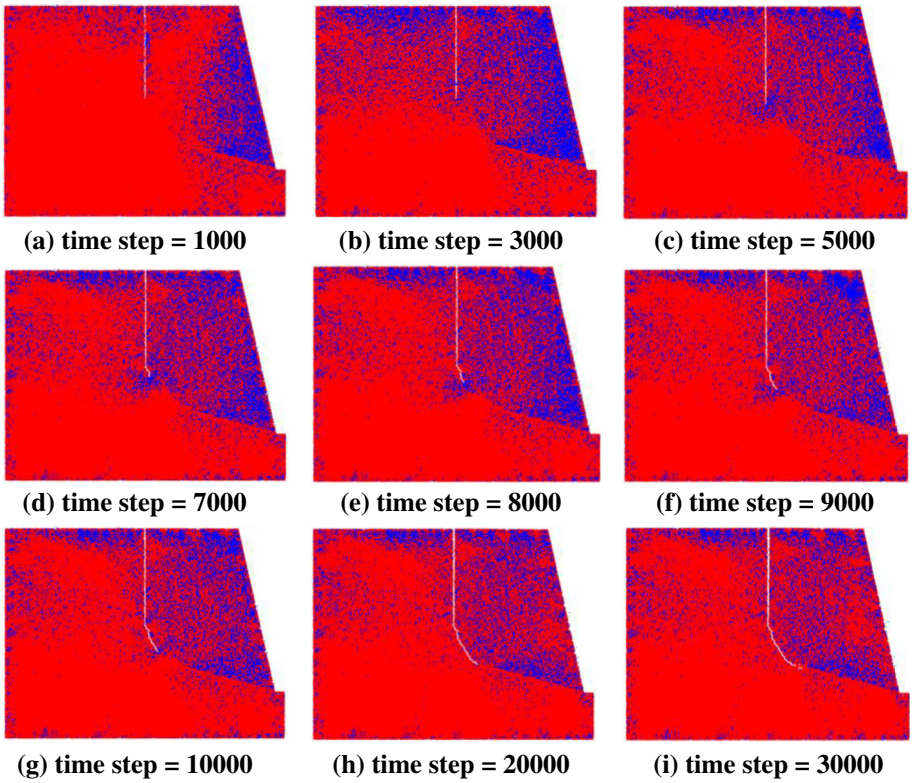

Fig. 3 (a)-(i) Evolution of the fracture trajectory and the corresponding force chain states. Red represents compression, and blue represents tension

The radius r of the failure path of the locked section can be expressed as:

$$r = \frac{y_t \cos\alpha}{1-\sin\alpha} - \frac{x_c \sin\alpha}{1-\sin\alpha} \tag{3}$$

The coordinates of the intersection point between the locked section and the creep section are assumed to be (x_1, y_1), which can be expressed as:

$$x_1 = y_t \cos\alpha - x_c \sin\alpha \tag{4}$$

$$y_1 = \frac{x_c \sin\alpha \cos\alpha}{1-\sin\alpha} - y_t \sin\alpha \tag{5}$$

The topographic line corresponding to the potential sliding body can be represented by the following function:

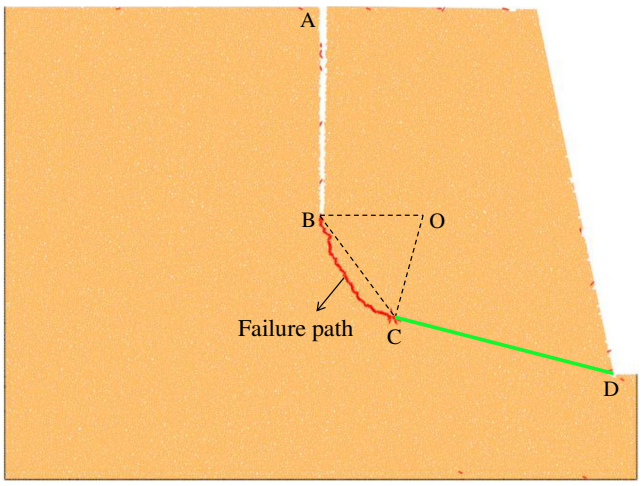

Fig. 4 Ultimate failure path of the locked section

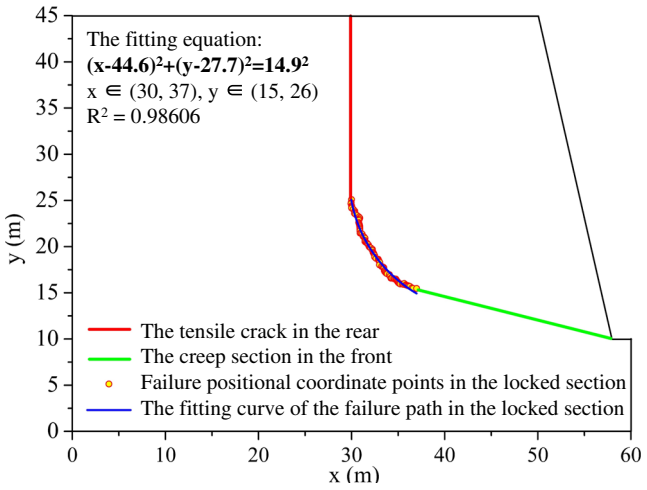

Fig. 5 Fitting analyses of the failure path in the locked section

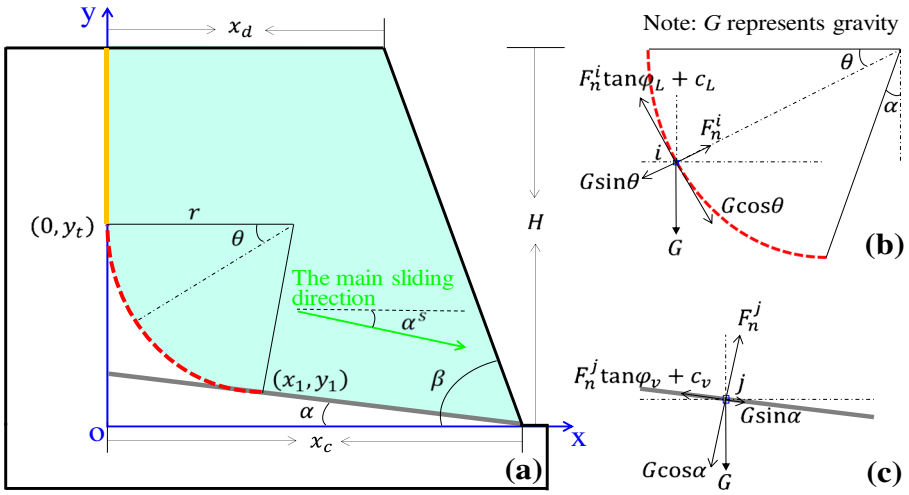

Fig. 6 (a)–(c) Generalized rockslide model and its corresponding parameters

$$y^o = \begin{cases} H & o \le x \le x_d \\ H + x_d \tan\beta - x\tan\beta & x_d < x \le x_c \end{cases} \tag{6}$$

where y^o represents the vertical coordinate of each point on the line.

Each point on the failure path of the locked section corresponds to a unique angular coordinate θ, the range of which is as follows:

$$\theta \in [o, \pi/2 - \alpha] \tag{7}$$

Therefore, the coordinates (x, y) of all points on the potential sliding surface composed of the failure path of the locked section and a part of the creep section can be represented by the following function:

$$y = \begin{cases} y_t - r\sin\theta & o \le x \le x_1 \\ x_c \tan\alpha - x\tan\alpha & x_1 < x \le x_c \end{cases} \tag{8}$$

The unit weight of the potential sliding body is γ. The cohesion and internal friction angle of the locked section in the limit state are denoted by c_L and ϕ_L, respectively. The cohesion and internal friction angle of the creep section in the limit state are similarly denoted by c_v and ϕ_v.

The direction of the sliding force is tangent to the potential sliding surface. The magnitude of the sliding force in the limit state is equal to that of the sliding resistance, which is determined by the Mohr-Coulomb criterion (Ge 2008). Therefore, if the sliding forces on the failure path of the locked section in the limit state are mapped to the x and y directions (Fig. 6b), the corresponding force magnitudes can be expressed as:

$$F_i^x = \int_o^{\frac{\pi}{2}-\alpha} [\gamma(y^o - y)\sin^2\theta \tan\phi_L r + c_L r]\sin\theta d\theta \tag{9}$$

$$F_i^y = \int_o^{\frac{\pi}{2}-\alpha} [\gamma(y^o - y)\sin^2\theta \tan\phi_L r + c_L r]\cos\theta d\theta \tag{10}$$

For the part of the potential sliding surface corresponding to part of the creep section, the sliding forces in the limit state can also be mapped to the x and y directions (Fig. 6c), and the corresponding force magnitudes can be expressed as:

$$F_j^x = \int_{x_1}^{x_c} [\gamma(y^o - y)\cos\alpha \tan\phi_v + c_v \sec\alpha]\cos\alpha dx \tag{11}$$

$$F_j^y = \int_{x_1}^{x_c} [\gamma(y^o - y)\cos\alpha \tan\phi_v + c_v \sec\alpha]\sin\alpha dx \tag{12}$$

The intersection angle α^s between the main sliding direction of the whole potential sliding body and the positive direction of the x-axis can be expressed as:

$$\alpha^s = \arctan\left(\frac{F_i^y + F_j^y}{F_i^x + F_j^x}\right) \tag{13}$$

The antisliding force on the failure path of the locked section consists of two components, i.e., F_{i1}^a from the shear strength of the locked section and F_{i2}^a from the component of gravity along the direction perpendicular to the sliding surface. These components can be respectively expressed as:

$$F_{i1}^a = \int_o^{\frac{\pi}{2}-\alpha} [\gamma(y^o - y)\sin^2\theta \tan\phi_L r + c_L r]\cos\left(\alpha^s + \theta - \frac{\pi}{2}\right) d\theta \tag{14}$$

$$F_{i2}^a = \int_o^{\frac{\pi}{2}-\alpha} \gamma(y^o - y)\sin^2\theta \sin\left(\left|\alpha^s + \theta - \frac{\pi}{2}\right|\right) r d\theta \tag{15}$$

The sliding force on the failure path of the locked section also consists of two components, i.e., F_{i1}^s from the component of gravity along the direction tangent to the sliding surface and F_{i2}^s

from the reaction force F_n^i of the sliding bed, as shown in Fig. 6b. These components can be respectively expressed as:

$$F_{i1}^s = \int_0^{\frac{\pi}{2}-\alpha} \gamma(y^o - y)\cos\theta\cos\left(\alpha^s + \theta - \frac{\pi}{2}\right) r\sin\theta d\theta \quad (16)$$

$$F_{i2}^s = \int_0^{\frac{\pi}{2}-\alpha} \gamma(y^o - y)\sin^2\theta\sin\left(\left|\alpha^s + \theta - \frac{\pi}{2}\right|\right) r d\theta \quad (17)$$

Similarly, for the part of the potential sliding surface corresponding to part of the creep section, the antisliding force components F_{j1}^a and F_{j2}^a and the sliding force components F_{j1}^s and F_{j2}^s can be respectively expressed as:

$$F_{j1}^a = \int_{x_1}^{x_c} [\gamma(y^o - y)\cos\alpha\tan\phi_v + c_v\sec\alpha]\cos(\alpha^s - \alpha) dx \quad (18)$$

$$F_{j2}^a = \int_{x_1}^{x_c} \gamma(y^o - y)\cos\alpha\sin(\alpha^s - \alpha) dx \quad (19)$$

$$F_{j1}^s = \int_{x_1}^{x_c} \gamma(y^o - y)\sin\alpha\cos(\alpha^s - \alpha) dx \quad (20)$$

$$F_{j2}^s = \int_{x_1}^{x_c} \gamma(y^o - y)\cos\alpha\sin(\alpha^s - \alpha) dxo \quad (21)$$

The stability coefficient F_s can thus be expressed as:

$$F_s = \frac{F_{i1}^a + F_{i2}^a + F_{j1}^a + F_{j2}^a}{F_{i1}^s + F_{i2}^s + F_{j1}^s + F_{j2}^s} \quad (22)$$

The potential sliding body is in the limit equilibrium state when $F_s = 1$, and the corresponding y_t can be used to determine the critical tension crack depth H_{cr} via the following equation:

$$H_{cr} = H - y_t \quad (23)$$

It is evident that H_{cr} is a function of nine independent variables: the slope height, H; the distance between the tension crack and the edge of the slope face, x_d; the dip angle of the creep section, α; the slope angle, β; the unit weight of the potential sliding body, γ; the cohesion of the locked section in the limit state, c_L; the internal friction angle of the locked section in the limit state, ϕ_L; the cohesion of the creep section in the limit state, c_v; and the internal friction angle of the creep section in the limit state, ϕ_v. Thus, this function can be represented as follows:

$$H_{cr} = f(H, x_d, \alpha, \beta, \gamma, c_L, \phi_L, c_v, \phi_v) \quad (24)$$

Optimized model

The real topographic profile of a specific potential rockslide area (Fig. 7) can usually be captured reasonably accurately based on measurements performed by an unmanned aerial vehicle of the actual profile of the slope. Hence, the topographic line described by Eq. (6) can be replaced by a more precise topographic function y^o. Similarly, the x_c in the optimized model shown in Fig. 7 can be measured directly instead of being expressed in terms of x_d and β, as shown in Eq. (2). After this optimization, H_{cr} is a function of the following nine independent variables: the slope height, H; the horizontal distance between the tension crack and the toe point, x_c; the dip angle of the creep section, α; the unit weight of the potential sliding body, γ; the cohesion of the locked section in the limit state, c_L; the internal friction angle of the locked section in the limit state, ϕ_L; the cohesion of the creep section in the limit state, c_v; the internal friction angle of the creep section in the limit state, ϕ_v; and the topographic function y^o. Hence, this function can be represented as follows:

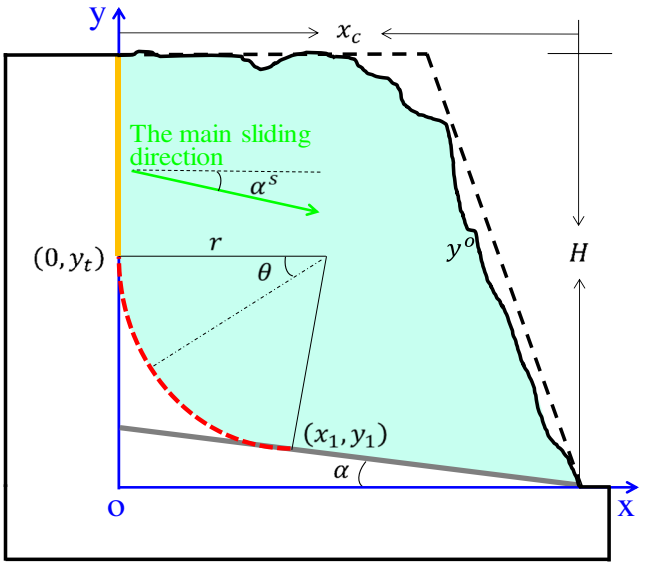

Fig. 7 Optimized model with the actual topographic profile

$$H_{cr} = f(H, x_c, \alpha, \gamma, c_L, \phi_L, c_v, \phi_v, y^o) \quad (25)$$

Solution process

For a rockslide that conforms to the three-section mechanism, the process of solving for H_{cr}, as shown in Fig. 8, corresponds to the propagation of the tension crack at the trailing edge and includes the following steps:

1) Input the relevant data for a specific rock slope as collected from field studies and/or documented information on the case.
2) Initialize ξ and δ, where ξ is a reduction coefficient associated with tension crack propagation and δ is a coefficient determining the calculation accuracy. The recommended values of ξ and δ are 10,000 and 0.0001, respectively.
3) Initialize the y-coordinate y_t of the tip point of the tension crack and then reduce the value of this parameter to reflect tension crack propagation.

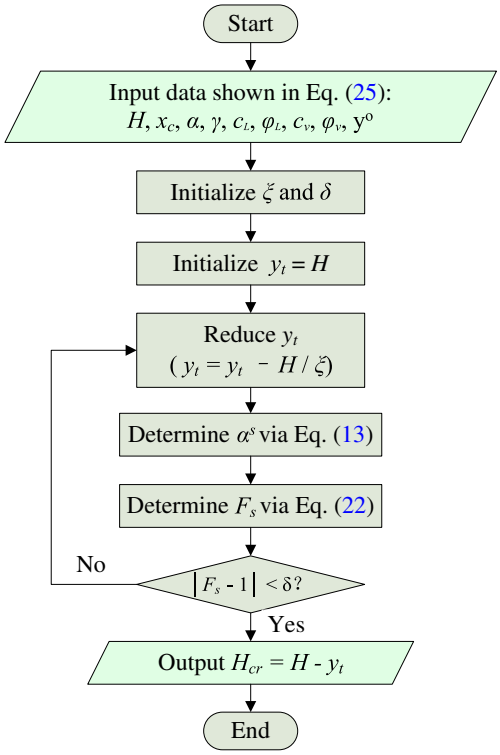

Fig. 8 Process flow diagram for solving for H_{cr}

4) Determine α^s using Eq. (13), for which the intermediate parameters can be acquired from Eqs. (2)–(12).
5) Determine F_s using Eq. (22), for which the intermediate parameters can be acquired from Eqs. (14)–(21).
6) Output H_{cr}, as expressed in Eq. (23), if $|F_s - 1| < \delta$; otherwise, further reduce y_t in accordance with step 3, and then, repeat steps 4 and 5 until $|F_s - 1| < \delta$.

Case study

The typical slope selected for this case study is located on the left bank of the dam area of the Laxiwa hydropower station in Qinghai province, China. It was identified in a feasibility study of the dam site before the year of 1991 and was called deformation body II (Fig. 9). A comprehensive geological engineering exploration revealed that deformation body II is a potential rockslide area conforming to the three-section mechanism (Huang et al. 1991). The lithology of the slope is grayish white massive granite with a medium coarse-grained texture, which can be regarded as a homogeneous rock mass. The creep section was formed by a small fault, Hf_4. This fault is exposed on the slope surface and was successfully traced by means of two exploration adits, numbered $P_D^{\#}15$ and $P_D^{\#}3$. The fault zone of Hf_4 is composed of breccia and purplish red fault gouge and is characterized by evident gravity creep phenomena: complex components, a disordered structure, argillaceous filling, and poor cementation, including fine structural breccia. The microscopic characteristics of quartz particles in Hf_4 include the undulatory extinction, turbid crystals, and Tuttle deformation lamellas. The undulatory extinction is the sign of compressional structures. Turbid crystals and Tuttle deformation lamellas are products of the mechanical mixtures entering crystal defects and lattice slip surfaces during the gravity creep deformation, respectively. In addition, significant derivative deformations exist on the two sides of Hf_4, fresh, short, unfilled, and open pinnate cracks. The rock mass above Hf_4 exhibits strong loosening and is relatively broken, whereas that below Hf_4 is integrated. Thus, only the small area near the entrance of adit PD#3 needed support measures, while the lengths of support required in adit PD#15 and PD#17 are 30 m and 15 m near the entrance of the exploration, respectively. Deformation phenomena of bending and tension cracking in the rock mass were found at the top of the slope, resulting in a tensile collapse belt with a width of 10 m at the position of the tension crack. The tension crack was also found in adit $P_D^{\#}17$, the opening width of which was 5–10 cm, with the obvious exhaust phenomenon indicating that the crack has penetrated between adit $P_D^{\#}17$ and the slope surface. However, the tension crack had failed to propagate to the elevation of adit $P_D^{\#}15$, indicating the existence of a locked section between the tip of the tension crack and fault Hf_4.

Critical tension crack depth

For the establishment of a Cartesian coordinate system similar to that in Fig. 7 for deformation body II, the topographic function can be accurately represented as shown in Eq. (26).

$$y^o = \begin{cases} 208.8 + 0.34x & 0 \le x \le 7.6 \\ 215.64 - 0.56x & 7.6 < x \le 19.5 \\ 204.4275 + 0.015x & 19.5 < x \le 24.7 \\ 238.637 - 1.37x & 24.7 < x \le 38.5 \\ 228.242 - 1.1x & 38.5 < x \le 53.1 \\ 263.288 - 1.76x & 53.1 < x \le 60.0 \\ 493.688 - 5.6x & 60.0 < x \le 61.8 \\ 258.23 - 1.79x & 61.8 < x \le 76.3 \\ 204.82 - 1.09x & 76.3 < x \le 92.2 \\ 185.458 - 0.88x & 92.2 < x \le 110.2 \\ 253.782 - 1.5x & 110.2 < x \le 130.1 \\ 157.508 - 0.76x & 130.1 < x \le 168.4 \\ 164.5808 - 0.802x & 168.4 < x \le 191.0 \\ 248.0478 - 1.239x & 191.0 < x \le 200.3 \end{cases} \quad (26)$$

The relevant physical and mechanical parameters (Huang et al. 1991) are shown in Table 3. The parameters c_L and ϕ_L correspond to the residual strength of the granite. The parameters c_v and ϕ_v correspond to the long-term strength of Hf_4. Thus, H_{cr} can be calculated using the methodology proposed in the previous section. The necessary calculations were conducted in the numerical computing environment of MATLAB (MATrix LABoratory). The calculation program was compiled in accordance with the equations of the theoretical model given above and the process flow diagram shown in Fig. 8. After the relevant data shown in Table 2 and Eq. (26) were input, the reduction coefficient ξ and the accuracy coefficient δ were set to 10,000 and 0.0001, respectively. The y-coordinate y_t of the tip point of the tension crack was initialized to 211.4 m. As shown in Fig. 8, the values of α^s and F_s were iteratively calculated after the reduction of y_t (subtracting H/ξ each time); this process was implemented by means of loop statements in the calculation program. The range of H_{cr} was from

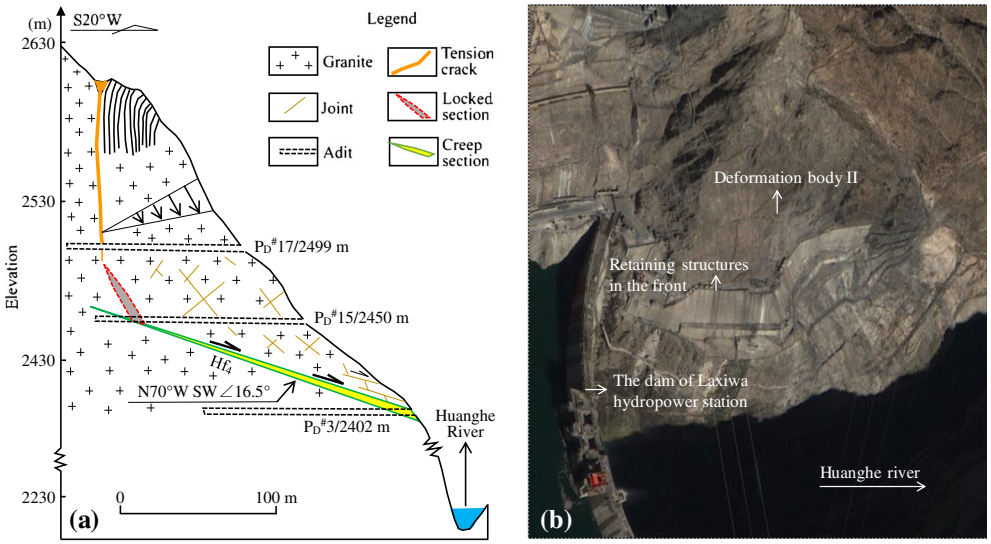

Fig. 9 Deformation body II at the Laxiwa hydropower station site in China. (a) The profile completed by Huang et al. (1991) before the hydropower construction. (b) The picture made by Google Earth in 2010 after the hydropower completion

111.1164 to 110.9339 m, corresponding to the F_s range of 0.9999 to 1.0001 determined by the value of δ. Therefore, the calculated result for H_{cr} can be taken to be 111 m. For comparison, the value of H_{cr} calculated using Eq. (1) is 94.7306 m.

To ensure the construction and operational safety of the hydropower station, active support measures have been applied to deformation body II to prevent further tension crack propagation. Thus, the precise value of H_{cr} cannot be known. However, the exploration adit $P_D^{\#}17$ shown in Fig. 9 revealed that the critical tension crack depth H_{cr} for the instability of this slope is greater than 101 m. Thus, it is evident that the H_{cr} value calculated via Eq. (25) is more reliable and accurate than the H_{cr} value calculated via the empirical equation shown in Eq. (1).

Parameter sensitivity analyses

Parameter sensitivity analyses were conducted to investigate the influence of parameter measurement error on the calculation results. The results shown in Fig. 10 illustrate how the critical tension crack depth changes as one geotechnical parameter is varied. The critical tension crack depth H_{cr} is negatively affected by the unit weight of the potential sliding body (γ) and the dip angle of the creep section (α), and it is positively affected by the other six parameters. Figure 10 shows that the value of H_{cr} is very sensitive to changes in the values of the slope height (H), the dip angle of the creep section (α), the cohesion of the locked section in the limit state (c_L), the internal friction angle of the locked section in the limit state (ϕ_L), and the internal friction angle of the creep section in the limit state (ϕ_v); is somewhat sensitive to changes in the values of the unit weight of the potential sliding body (γ) and the cohesion of the creep section in the limit state (c_v); and is relatively insensitive to the horizontal distance between the tension crack and the toe point (x_c). Therefore, ensuring the accuracy of the input parameters is critical for obtaining an exact value of the critical tension crack depth for providing early warning of rockslides.

Discussion

Real-time monitoring and early warning for landslides, especially rockslides that exhibit rapid development, are difficult to achieve. Rockslides that conform to the three-section mechanism are one class of rockslides that exhibit sudden instability. Displacement monitoring and early warning systems are difficult to successfully apply for these rockslides because the deformation monitoring curves usually show none of the characteristics of gradual variation that are used as the basis to trigger typical landslide warnings (Yin et al. 2010; Ju et al. 2015; Macciotta et al. 2016). However, the evolution of such rockslides must be closely associated with tension crack propagation. Thus, tension crack depth monitoring is a potential approach for early warning. However, for this approach to instability warning, it is vital to determine the tension crack depth that corresponds to the critical state for slope instability.

Initially, a corresponding threshold equal to half of the slope height was considered, in accordance with field observations. To improve the accuracy of the critical depth estimate, the empirical equation given in Eq. (1) was later summarized based on rockslides conforming to the three-section mechanism (Zhang and Liu 1990) and was recommended for predicting the instability of such rockslides (Huang 2012). As a further development of this

Table 3 Relevant parameters (Huang et al. 1991) and calculation results for the selected typical slope

H(m)	x_c(m)	$\alpha(^\circ)$	γ(kN/m^3)	c_L(MPa)	$\phi_L(^\circ)$	c_v(MPa)	$\phi_v(^\circ)$	H_{cr}(m)
211.4	200.3	16.5	26.5	0.5	32	0.027	13.64	111

Note: H_{cr} calculated via Eq. (1) is 94.73 m and the adit exploration indicated that H_{cr} > 101 m

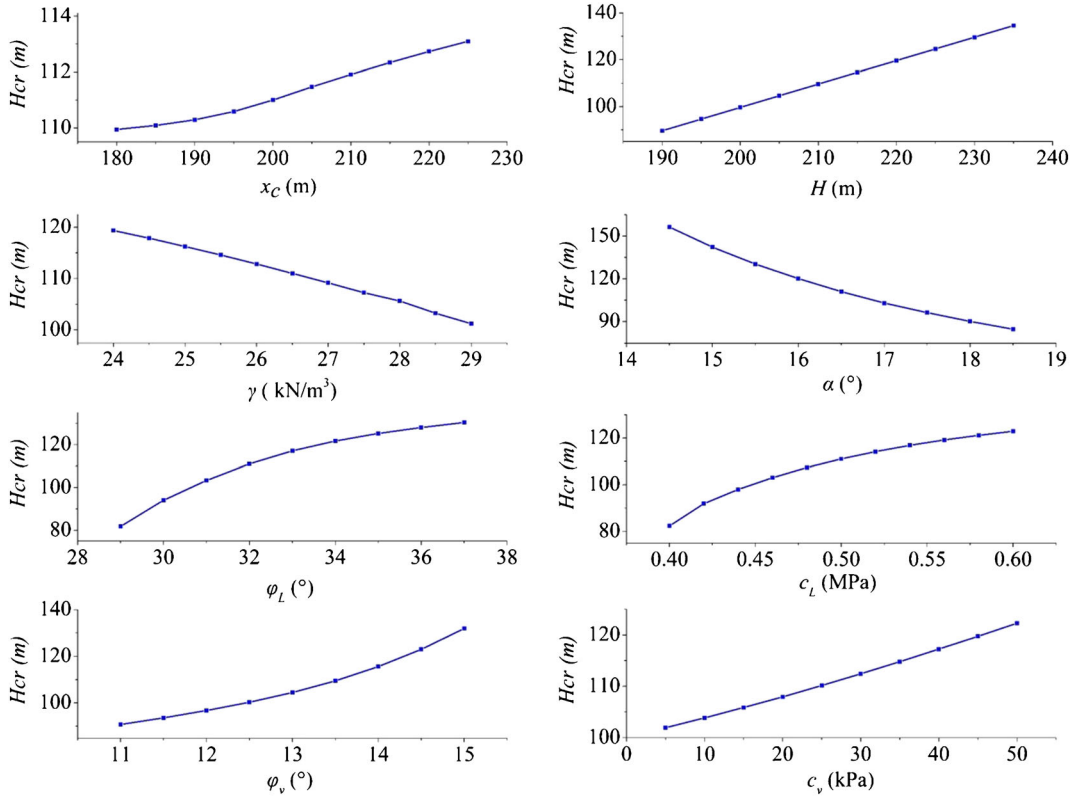

Fig. 10 Sensitivity of the critical tension crack depth to the slope parameters in the case study

pioneering approach, the new methodology proposed in this paper has a clear theoretical basis and offers higher accuracy; thus, it is significant for improving early warning capabilities for such landslides. In addition, the new methodology is feasible and practical because all nine independent variables on which it relies can be easily measured. Notably, the slope height in this paper is the elevation difference relative to the creep section. The mechanical parameters of the creep section in the limit state should be considered to correspond to the long-term strength, as they reflect the previous creep, whereas the residual shear strength parameters of the locked section correspond to the limit stability state. If the precise topographic function y^o cannot be obtained, then H_{cr} can be calculated instead using Eq. (24) based on the parameters shown in Fig. 6; this calculation is suitable for simple and rapid assessment in geological engineering surveys.

Although the new methodology proposed in this paper represents evident progress relative to the previous approach, it is still difficult to ensure that its results are absolutely accurate. The main reasons are as follows: (1) to make the problem solvable, many assumptions are adopted in the modeling and solution process and (2) the accuracy of the calculation results strongly depends on the accuracy of the measured parameter values. In a real rockslide that conforms to the three-section mechanism, the rock mass in the locked section is usually not absolutely homogeneous. The tiny heterogeneous behavior could result in the formation of a relatively rougher failure path in the locked section to increase the stability. Additionally, the numerical and theoretical models in this paper are both two-dimensional, neglecting the contribution of lateral boundaries to the stability. Therefore, the homogeneity assumption and 2D limitation may make the calculated threshold be conservative, i.e., smaller than the actual value. In the future, we will continue to focus on research related to the real-time monitoring and early warning of the actual rockslides of this type to further optimize the proposed methodology and improve the accuracy of the calculated critical threshold.

Conclusions

A new methodology has been proposed in this paper for calculating the critical tension crack depth at the trailing edge of a rockslide that conforms to the three-section mechanism in order to improve stability analyses, instability prediction, and early warning for such rockslides. The following conclusions can be drawn:

1. Based on a numerical simulation conducted using PFC^{2D}, the results of field investigations indicating that the failure path of the locked section is a circular arc instead of a straight-line path have been verified.
2. The critical threshold of the tension crack depth for slope instability has been derived based on the limit equilibrium theory, and the result shows that this threshold is not only related to the slope height but also closely related to other geometric and mechanical parameters of the slope including the following: the position of the tension crack relative to the

slope face, the dip angle of the creep section, the unit weight of the potential sliding body, the cohesion and internal friction angle of the locked section corresponding to the residual strength, the cohesion and internal friction angle of the creep section corresponding to the long-term strength, and the slope topography.

3. In a typical case study, the critical threshold of the tension crack depth was found to be greater than 101 m through field investigations. The result calculated using the previous empirical equation is 94.7306 m, while the result calculated using the methodology proposed in this paper is 111 m. Thus, this case study verifies the correctness of the new methodology and shows that it yields a more accurate result than the previous empirical equation.

Funding information

This research was financially supported by the National Key R&D Program of China (2017YFC1501301) and the National Natural Science Foundation of China (Grant Nos. 41972284 and 41521002). This work was also supported by funding from the China Railway Eryuan Engineering Group Co., Ltd. (KYY2019066(19-20)) and the research fund of the State Key Laboratory of Geohazard Prevention and Geoenvironment Protection (No. SKLGP2019Z016).

References

Bishop AW (1955) The use of the slip circle in the stability analysis of slopes. Geotechnique 5(1):7–17

Cho N, Martin CD, Sego DC (2007) A clumped particle model for rock. Int J Rock Mech Min Sci 44:997–1010

Duncan JM (1996) State of the art: limit equilibrium and finite-element analysis of slopes. J Geotech Geoenviron Eng 122(7):577–596

Eberhardta E, Steadb D, Cogganc JS (2004) Numerical analysis of initiation and progressive failure in natural rock slopes—the 1991 Randa rockslide. Int J Rock Mech Min Sci 41:69–87

Fredlund DG, Krahn J (1977) Comparison of slope stability methods of analysis. Can Geotech J 14:429–439

Fu XD, Sheng Q, Zhang YH, Chen J, Zhang SK, Zhang ZP (2017) Computation of the safety factor for slope stability using discontinuous deformation analysis and the vector sum method. Comput Geotech 92:68–76

Ge XR (2008) Deformation control law of rock fatigue failure, real-time X-ray CT scan of geotechnical testing and new method of stability analysis of slopes and dam foundations. Chin J Geotech Eng 30(1):1–20

Griffiths DV, Lane PA (1999) Slope stability analysis by finite elements. Geotechnique 49(3):387–403

Guo MW, Liu SJ, Yin SD, Wang SL (2018) Stability analysis of the Zhangmu multi-layer landslide using the vector sum method in Tibet, China. Bull Eng Geol Environ 78:4187–4200. https://doi.org/10.1007/s10064-018-1386-3

Guo MW, Li CG, Wang SL, Yin SD, Liu SJ, Ge XR (2019) Vector-sum method for 2D slope stability analysis considering vector characteristics of force. Int J Geomech 19(6):04019058. https://doi.org/10.1061/(ASCE)GM.1943-5622.0001436

Huang RQ (2009) Some catastrophic landslides since the twentieth century in the southwest of China. Landslides 6(1):69–81

Huang RQ (2012) Mechanisms of large-scale landslides in China. Bull Eng Geol Environ 71(1):161–170

Huang RQ, Deng RG (1993) Full simulation process for high slope substance moving. Chengdu University of Technology Press, Chengdu (in Chinese)

Huang RQ, Zhang ZY, Wang ST (1991) Systematic engineering geology studying of the stability of high slope. Chengdu University of Technology Press (in Chinese)

Huang D, Cen DF, Ma GW, Huang RQ (2015) Step-path failure of rock slopes with intermittent joints. Landslides 12(5):911–926

Itasca Consulting Group Inc. (2016) PFC2D particle flow code in 2 dimensions user's guide

Ju NP, Huang J, Huang RQ, He CY, Li YR (2015) A real-time monitoring and early warning system for landslides in Southwest China. J Mt Sci 12(5):1219–1228

Liu GY, Zhuang XY, Cui ZQ (2017) Three-dimensional slope stability analysis using independent cover based numerical manifold and vector method. Eng Geol 225:83–95

Macciotta R, Hendry M, Martin CD (2016) Developing an early warning system for a very slow landslide based on displacement monitoring. Nat Hazards 81:887–907

Sartori M, Baillifard F, Jaboyedoff M, Rouiller JD (2003) Kinematics of the 1991 Randa rockslides (Valais, Switzerland). Nat Hazards Earth Syst Sci 3:423–433

Tang P, Chen GQ, Huang RQ, Zhu J (2020) Brittle failure of rockslides linked to the rock bridge length effect. Landslides 17:793–803

Yang SQ, Huang YH, Jing HW, Liu XR (2014) Discrete element modeling on fracture coalescence behavior of red sandstone containing two unparallel fissures under uniaxial compression. Eng Geol 178:28–48

Yin YP, Wang HD, Gao YL, Li XC (2010) Real-time monitoring and early warning of landslides at relocated Wushan Town, the Three Gorges Reservoir, China. Landslides 7:339–349

Zhang ZY, Liu HC (1990) Key engineering geology problem and research on Longyangxia Hydropower Station of Huanghe River. Chengdu University of Technology Press, Chengdu (in Chinese)

Zienkiewicz OC, Humpheson C, Lewis RW (1975) Associated and non-associated visco-plasticity in soil mechanics. Geotechnique 25(4):671–689

G. Chen · P. Tang · R. Huang (✉)
State Key Laboratory of Geohazard Prevention and Geoenvironment Protection,
Chengdu University of Technology,
Chengdu, 610059, China
Email: hrq@cdut.edu.cn

G. Chen
e-mail: chgq1982@126.com

P. Tang
e-mail: 270301316@qq.com

D. Wang · Z. Lin
China Railway Eryuan Engineering Group Co., Ltd,
Chengdu, 610031, China

D. Wang
e-mail: 99927394@qq.com

Z. Lin
e-mail: 759036719@qq.com

D. Huang
School of Civil and Transportation Engineering,
Hebei University of Technology,
Tianjin, 300401, China
e-mail: dahuang@hebut.edu.cn